Cavity Flow Over a Transonic Weapon Bay During Door Operation

G.J.M. Loupy[1] , G.N. Barakos[2]

CFD Laboratory, University of Glasgow, Glasgow, G12 8QQ, UK

N.J. Taylor[3]

MBDA UK Ltd, Filton, Bristol, BS34 7QW, UK

Abstract

This paper considers a transonic, idealised, weapon bay. The doors were either fixed, or opened in a dynamic way. The flow evolved in three stages during door opening, corresponding to closed cavity flow, transitional flow, and finally open cavity flow. The transition needs to be taken into account to design structures, as the bay wall loads were amplified, as well as the noise. The flow fluctuations, were also larger than for the fully established flow. The doors limited the development of the shear layer, at the early stage of the door opening.

[1]PhD Student. g.loupy.1@research.gla.ac.uk

[2]Professor, MAIAA, MRAeS, MAHS. george.barakos@glasgow.ac.uk, corresponding author

[3]Capability Leader, MBDA UK Ltd. nigel.j.taylor@mbda.co.uk

Latin

a	Wavelet dilatation or scale (1/s)
b	Wavelet translation parameter (s)
c	Sound speed (m/s)
C_l, C_m, C_n	Rolling, pitching and yawing moment coefficient (-)
C_x, C_y, C_z	Axial, side and normal force coefficient (-)
C_p	Pressure coefficient (-)
D	Cavity depth (m)
f	Frequency (Hz)
f_m	Frequency of the cavity mode m (Hz)
i, j, k	Cell index (m)
k	Specific turbulent kinetic energy (m^2/s^2)
DI	Noise Directivity (dB)
I	Local Noise Intensity (W/m2)
L	Cavity length (m)
m	Rossiter mode number (-)
M_∞	Free-stream Mach number (-)
N	Number of timestep (-)
p	Static pressure (Pa)
p'	Unsteady static pressure (Pa)
p_{ref}	International standard minimum audible sound (Pa)
p_{RMS}	Root mean square of pressure (Pa)
Q	Shear layer momentum (-)
Q_f	Noise Directivity Factor (-)

$\mathbf{R}_{i,j,k}$	Flux residual
Re_L	Reynolds number based on cavity length (-)
S	Reference Area (m^2)
St	Strouhal number (-)
t	Time (s)
u, v, w	Velocity components (m/s)
$\bar{U}$	Time Averaged Velocity (m/s)
U_∞	Free-stream Velocity (m/s)
U_{RMS}	Root Mean Square Velocity (m/s)
$V_{i,j,k}$	Volume of the cell i,j,k (m^3)
W	Cavity width (m)
W_Ψ^y	Wavelet transform
$\mathbf{w}_{i,j,k}$	Vector of conservative variable
X, Y, Z	Cartesian coordinates (m)
Greek	
α	Phase shift (-)
κ_ν	Constant dependent on cavity geometry and test conditions (-)
γ	Ratio of specific heats (-)
ω	Specific turbulence dissipation rate (1/s)
ω_0	Pulsation (1/s)
ϕ	Door angle (deg)
$\Psi(t)$	Mother wavelet (-)
ρ	Density (kg/m^3)

Greek

ρ_∞	Free-stream density (kg/m^3)
θ	Momentum thickness (m)

Acronyms

ALE	Arbitrary Lagrangian Eulerian
BILU	Block Incomplete Lower-Upper
BIW	Banded Integrated Wavelet
CFD	Computational Fluid Dynamics
CFL	CourantFriedrichsLewy
DDES	Delayed Detached-Eddy Simulation
HMB	Helicopter Multi-Block
LIC	Linear Integral Convolution
MUSCL	Monotone Upwind Schemes for Scalar Conservation Laws
NED	North East Down
OASPL	Overall Sound-Pressure Level
PSD	Power Spectral Density
RK4	Runge-Kutta method
RMS	Root Mean Square
SAS	Scale Adaptive Simulation
SPL	Sound-Pressure Level
UCAV	Unmanned Combat Air Vehicle
URANS	Unsteady Reynolds-Averaged Navier-Stokes

1 Introduction

Modern military aircraft and Unmanned Combat Air Vehicles (UCAVs) use weapon bays for stealth. When weapon bay doors are open at transonic conditions, the flow shear layer detaches from the front lip, breaks down, and interacts with the aft bay wall, producing reflected acoustic waves [1, 2], that influence the shear layer. This feedback loop tends to generate a strong acoustic field that comprises broadband noise and tones, called Rossiter modes [3]. These tones vary, depending on the geometry of the bay, the flow regimes they are subjected to, and the presence of stores. However, most of the published works addressed ideal cavities without complex design features [4], and real aircraft cavities only recently received attention [5, 6, 7]. The objective of this work is to approach the problem in a systematic way, by adding realism step by step from an ideal cavity. This paper shows a first step, by adding doors dynamically moving.

During the store release process, the doors open and then close, affecting the cavity flow. Adding fixed opened doors to complex [7], and ideal cavities [8, 9, 10] resulted in a dramatic amplification of the cavity acoustics. Half opened doors [5, 6, 7, 10] reduced the broadband noise and amplified the feedback loop under the covered part of the cavity, leading to stronger tones. Most cavities studies so far, are conducted in wind tunnels giving limited measurements of the flowfield. On the other hand, CFD computations result in the complete flowfield, and allow to develop an understanding of the flow physics involved. Due to the flow unsteadiness in weapon bay, there is

variability in the trajectories of released stores. The effect of the bay doors on the separation of a store had been experimentally studied by the end of the 80' by Blair *et al.*[11]. The doors were held at 48, 90, and 135 degrees. The cases at 48 and 135 degrees showed similar loads to the no door configuration. However, the case at 90 degrees showed amplification of the flow fluctuations [7, 8, 9]. Studies of the effect of door configurations than other 90 degrees are also discussed in [10, 12] (See also table 1).

Full scale fighter planes open their bays in about a second, and clear stores a few seconds later. During the door opening, the cavity flow is being established, and understanding the flow physics involved, may help optimise the store release process, minimising the effect of the flow fluctuations on the store, and supporting a safe, and stealthy store separation. The cavity flow establishment during the door opening is not yet addressed in the literature, and no experiments are published for CFD validation, as the geometric scaling makes a realistic opening difficult in wind tunnels. The influence of the doors on the cavity flow has so far been researched for moving doors by Sheta *et al.*[10] using CFD. It was shown that the OASPL level reached a peak at 30 degrees of door opening.

In this paper, the cavity flow is computed with the Scale Adaptive Simulation (SAS) method [13, 14] that has been successfully used for cavity flows with and without doors with the HMB flow solver [15]. The paper is organised as follows: A description of the CFD methodology used for the computations is first presented in section 2. Section 3 explains the post-processing methods used for the presentation of the results. The geometry

of the model, the flow conditions, and the axes convention are presented in section 4. Section 5 shows the validation of the HMB3 solver, and the results from which conclusions are drawn are given section 6.

Author	Method	Cavity	L/D mean	Mach	Configurations
Sheta [10] (2017)	DDES (Loci/CHEM)	Ideal Cavity	6.0	1.44	45, 90 and half open bay and dynamic between 5 and 35 degrees
Blair [11] (1989)	Experimental	Ideal Cavity	14	1.70 2.00 2.65	48, 90 and 135 deg and sliding door with moving store
Bacci [12] (2015)	DDES (Fluent)	UCAV 1303 with M219 bay	5.66	0.85	90 and 135deg fixed doors

Table 1: Works about door effect on the cavity flows at different angles.

2 CFD Methodology

The Helicopter Multi-Block (HMB3) [16] code is used for the present work. HMB3 solves the Unsteady Reynolds (Favre) Averaged Navier-Stokes (URANS) equations in integral form using the arbitrary Lagrangian Eulerian (ALE) formulation, first proposed by Hirt *et al.* [17], for time-dependent domains, which may include moving boundaries. The Navier-Stokes equations are discretized using a cell-centered finite volume approach on a multi-block grid. The spatial discretization of these equations leads to a set of ordinary differ-

ential equations in time,

$$\frac{d}{dt}(\mathbf{w}_{i,j,k}V_{i,j,k}) = -\mathbf{R}_{i,j,k}(\mathbf{w}) \tag{1}$$

where i, j, k represent the cell index, $\mathbf{w}$ and $\mathbf{R}$ are the vector of conservative variables and flux residual respectively and $V_{i,j,k}$ is the volume of the cell i, j, k. To evaluate the convective fluxes, the Osher [18] and Roe [19] approximate Riemann solvers are used and the viscous terms are discretised using a second order central differencing spatial discretization. The Monotone Upstream-centered Schemes for Conservation Laws (MUSCL) of Leer [20], is used to provide third order accuracy in space. The HMB3 solver uses the alternative form of the Albada limiter [21] activated in regions where large gradients are encountered due to shock waves, avoiding non-physical, spurious oscillations. An implicit dual-time stepping method is employed to performed the temporal integration, where the solution is marching in pseudo-time iterations to achieve fast convergence, which is solved using a first-order backward difference. The linearized system of equations is solved using the Generalized Conjugate Gradient method with a Block Incomplete Lower-Upper (BILU) factorization as a pre-conditioner [22]. The implicit scheme requires a small CFL at the early iterations or some explicit iteration using the forward Euler or four stage Runge-Kutta (RK4) methods [23]. Multi-block structured meshes are used with HMB3, which allow an easy sharing of the calculation load for parallel execution. The structured multi-block hexa meshes are generated using the ICEM-Hexa$^{\text{TM}}$tool of ANSYS. An overset grid method is available in HMB3 [24], to allow relative

motion between mesh components. The chimera method is based on composite grids, consisting of independently generated, overlapping non-matching sub-domains. Each of these sub-domains are referred to as a Level and are sorted hierarchically, with higher levels having priority[24]. The exchange of information between sub-domains is achieved through interpolation and by following the level hierarchy.

3 Post-Processing and Analysing Methods

This section presents the techniques used to analyse the unsteady flow data. CFD flow-field files are written at specific instances in time, and flow "probes" at specific mesh points are sampled at every time step. The probe pressure signals are first analysed using the Power Spectral Density (PSD), described in the paper of Babu *et al.*[25]. The variation in static pressure levels was studied using the Root-Mean-Square (RMS) of the unsteady pressure:

$$p'_{RMS} = \sqrt{\sum_{n=1}^{N} \frac{(p - \overline{p})^2}{N}} \tag{2}$$

with N the number of timesteps. Although p'_{RMS} is measured in Pascals, it is customary in cavity flow studies to report it as the Overall Sound-Pressure Level (OASPL) [26]:

$$OASPL = 20 \text{ LOG}_{10} \left[\frac{p'_{RMS}}{p_{ref}} \right] \tag{3}$$

which has the units of decibels. p_{ref} is the international standard for the minimum audible sound, which has the value of 2×10^{-5} Pa [26].

The cavity tones are usually termed Rossiter modes [3], and a semi-empirical formula is available for the estimation of their frequencies. Rossiter, based the formula on experimental results over a range of Mach numbers from 0.4 to 1.4, and for various cavity aspect ratios. The modified version of the original formula by Heller [27] is as follows:

$$f_m = \frac{U_\infty}{L}\left[\frac{m-\alpha}{M_\infty\left(1+\left(\frac{\gamma-1}{2}\right)M_\infty^2\right)^{-1/2}+1/\kappa_\nu}\right] \tag{4}$$

where f_m is the frequency of mode m, U_∞ is the free-stream velocity, M_∞ is the free-stream Mach number, and L is the cavity length. The ratio of specific heats of the employed gas γ, the phase shift α, and the constant dependent on the cavity geometry and test conditions κ_ν, are respectively equal to 1.4, 0.25 and 0.57 at those conditions.

The fluctuations of the cavity flow are compared using the root mean square (RMS) of the velocities defined as:

$$U_{RMS} = \sqrt{\sum_{n=1}^{N}\frac{(U_n-\bar{U})^2}{N}} \tag{5}$$

The boundaries of the shear layer are defined as the strictly positive values of the shear layer momentum Q, product between the flow momentum, and the local contribution to the displacement thickness. The negative values due to the cavity flow re-circulation are imposed to zero:

$$Q = max\left(0, \frac{\rho u}{\rho_\infty U_\infty}\left(1-\frac{u}{U_\infty}\right)\right) \tag{6}$$

The thickness of the shear layer is given by the momentum thickness θ:

$$\theta(x,y) = \int_{-D}^{\infty} Q(x,y,z)\,\mathrm{d}z \tag{7}$$

with z the normal to the shear layer, and D the cavity depth.

3.1 Time Frequency Analysis - Morlet Wavelet Method

The cavity flow is unsteady, and its dynamics must be understood to gain insight in its physics. The continuous Morlet wavelet transform is a method for time-frequency analysis, that reveals the temporal fluctuations of the different frequencies present in the flow. This technique is used to show the fluctuations of the cavity modes during opening. The wavelet transform[28] $W_\Psi^y(f,t)$ is a convolution of the signal $s(t)' = s(t) - \overline{s}$ with a scaled mother wavelet $\Psi(t)$ conserving the sign of the signals in time and frequency:

$$W_\Psi^y(a,b) = \frac{1}{\sqrt{c_\Psi |a|}} \int_{-\infty}^{\infty} s'(t) \Psi \left(\frac{t-b}{a} \right) dt. \tag{8}$$

In the above equation, a is called the dilatation or the scale, b the translation parameter, $c_\Psi = \sqrt{\pi/\beta}$ and $\beta = \omega_0^2$. The dilatation a is related to the frequency f of the wavelet, the translation parameter b is related to the time shift t of the wavelet. The mother wavelet $\Psi(t)$ is given by :

$$\Psi(t) = e^{\frac{-\beta t^2}{2}} e^{j\omega t} \tag{9}$$

Band Integrated Wavelets (BIW) plots show the energy content within a particular frequency range and are calculated using the following equation:

$$BIW(t) = \int_{f_1}^{f_2} W_\Psi^y(f,t)^2 \tag{10}$$

where f_1 and f_2 are the lower and upper limits of the desired frequency range. The wavelets in decibel are given by:

$$W_{dB}(f,t) = 20 \ \mathrm{LOG}_{10} \left[\frac{W_\Psi^y(f,t)^2}{p_{ref}} \right] \tag{11}$$

The wavelet envelop is the amplitude of the frequency in time, and is determined using the maximum of the absolute value of the wavelet transform over windows equal to half of a period of the frequency.

3.2 Noise Directivity

The local noise intensity is defined as:

$$I = \frac{p'^2_{RMS}}{\rho c} \tag{12}$$

with ρ the density, and c the sound speed. A noise directivity factor is then defined as the ratio of the local noise intensity I divided by the average noise intensity I_{av} on the scanned surface:

$$Q_f = \frac{I}{I_{av}} \tag{13}$$

Then the directivity DI is computed on every CFD points of the scanned surface:

$$DI = 10log_{10}(Q_f). \tag{14}$$

The directivity depends both on the noise emitted by every point inside the cavity, and on the distribution of the noise sources.

4 Geometrical and Computational Model

Computations are performed with the HMB3 solver using the k-ω SAS turbulence model [13, 14]. The computational domain (Figure 1) includes solids walls 1.5 cavity length ahead and aft the cavity, followed by symmetry conditions. The domain is 8 cavity lengths long in the stream-wise direction.

The flow over a square cavity, of length to depth ratio of 7, and width to depth ratio of 2 is now discussed. This cavity is denoted as LD7. The cavity length is 3.59m, the freestream Mach number is 0.85, and the Reynolds Number based on the cavity length R_{eL} is 6.5 million (Figure 2). A non dimensional timestep of 0.01 is used, equivalent to one hundredth of a cavity travel time equivalent to 13ms for this case. The doors are modelled as solid flat plates with a thickness of 0.3% of the cavity depth, a width of 46% of the cavity width, and a length of 98% of the cavity length. These dimensions

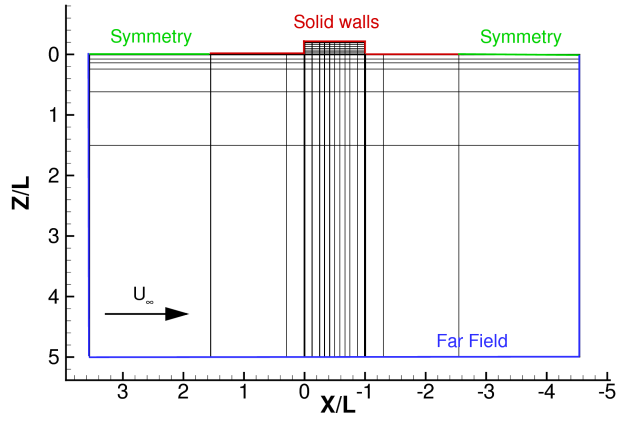

Figure 1: Boundary conditions and blocking at the mid-span of the computational domain.

allow for some cavity venting when doors are closed.

CFD results from different configurations with static doors are tested and compared against computations for dynamic opening (Table 2). Static door configurations consider cases at 20, 45, 90 and 110 degrees. The effects of the dynamic door opening are assessed, computing the door operation for angles between 0 and 110 degrees. Three opening frequencies were computed, 110,

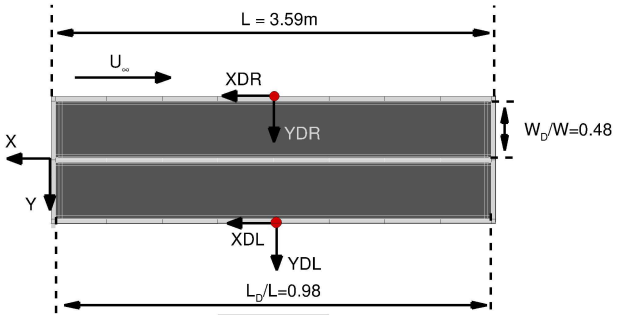

(a) Bottom view - Doors closed

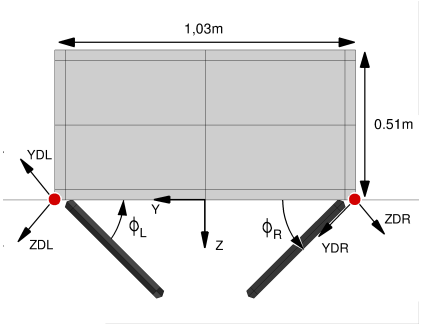

(b) Downstream view - Doors at 45 degrees

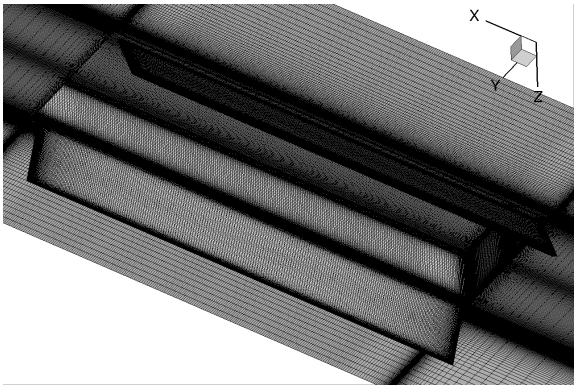

(c) Surface Mesh - Doors at 110 degrees

Figure 2: Schematic view of the vented cavity with store.

220 and 440 degrees/sec, respectively, equivalent to 80, 40 and 20 travel times at 3000 ft of altitude. They are respectively termed slow, medium and fast opening. Modern fighters complete the door opening during 1 second, for a cavity length of about 4 meters that corresponds in the CFD conditions to a Strouhal number of 0.027. The Strouhal number compares the door opening

Cavity	Angle (deg)	Angular vel. (deg/s)	Grid size (10^6 cells)	Cavity Travel Times
LD7	20	0	34.2	22
LD7	45	0	34.2	20
LD7	90	0	34.2	20
LD7	110	0	34.2	38
LD7	$0 \rightarrow 110$	110	34.2	40
LD7	$0 \rightarrow 110$	220	34.2	82
LD7	$0 \rightarrow 110$	440	34.2	40
LD7	No Doors	/	30.5	25
M219	90	0	13.2	25
M219	90	0	22.3	25
M219	90	0	33.9	25
M219	No Doors	/	30.2	25

Table 2: Details of the configurations run with SAS.

frequency f_d and the travel time frequency f_{tt} as:

$$St_{opening} = \frac{f_d}{f_{tt}} = \frac{f_d L}{U_\infty} \tag{15}$$

Where L is the cavity length, U_∞ is the air speed at the free-stream surrounding the cavity. The simulated slow, medium, and fast opening, give Strouhal numbers of 0.023, 0.047 and 0.094. The slow opening is perhaps the most representative of actual aircraft cavities, but faster studies are also considered, since to maintain stealth, the cavity exposure should be minimised. The computations begin with a transitional phase where the cavity flow settles. The first 10 cavity travel times of the flow, or equivalently 130ms, are ignored, and then, the flow is sampled and stored. The mesh is composed of one grid component per object (i.e. left door, right door, and cavity), and the chimera method was used. The characteristics of each grid component are given in table 3.

Name	Grid size (10^6 cells)	Number of blocks
Clean cavity	30.5	1010
Door	1.9	42

Table 3: Details of the grid components.

The force coefficients (C_{force}) and the moment coefficients (C_{moment}) are computed as:

$$C_{force} = \frac{F}{\frac{1}{2}\rho_\infty U_\infty^2 S} \tag{16}$$

$$C_{moment} = \frac{M}{\frac{1}{2}\rho_\infty U_\infty^2 L_{ref} S} \tag{17}$$

with F and M the force and moment on a component of interest (door, wall), L_{ref} the reference length, and S the reference area. The loads on the cavity and the doors are computed with $L_{ref} = D$, the cavity depth, and $S = WD$, the back wall area. The moment axes are indicated by red dots on figure 2. The cavity loads are presented in the North East Down (NED) system where X is positive north, Y is positive east and perpendicular to X axis, and Z is positive towards the earth centre. The door system is right handed and coincident with the NED system at closed position, with respect to the roll, pitch, and yaw axes.

Validation of SAS for cavity flow computation, is carried out for the M219 cavity [29]. M219 has a length to depth ratio of 5, a width to depth ratio of 1, and a length of 0.51m. The experiments were carried out by Nightingale *et al.*[29] at a Mach Number of 0.85, and Reynolds R_{eL} of 6.5 million. The cavity had two doors attached at its sides at an angle of 90 degrees. Pressure data were obtained using Kulite^{TM} pressure transducers at the cavity ceiling. Three grid densities of 13, 22 and 34 million points are compared to the experimental data (Figure 3) at conditions of table 2.

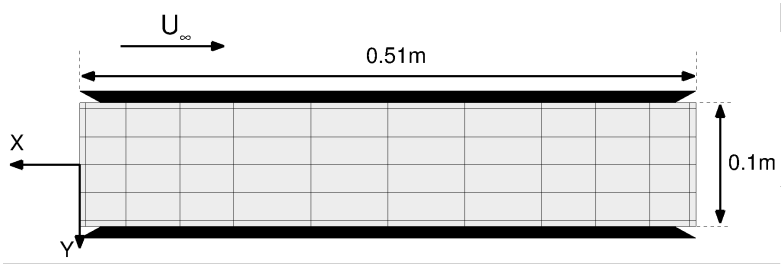

(a) Bottom view

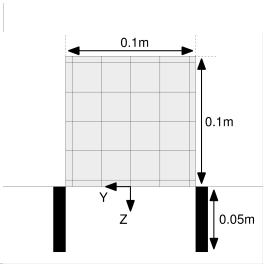

(b) Downstream view

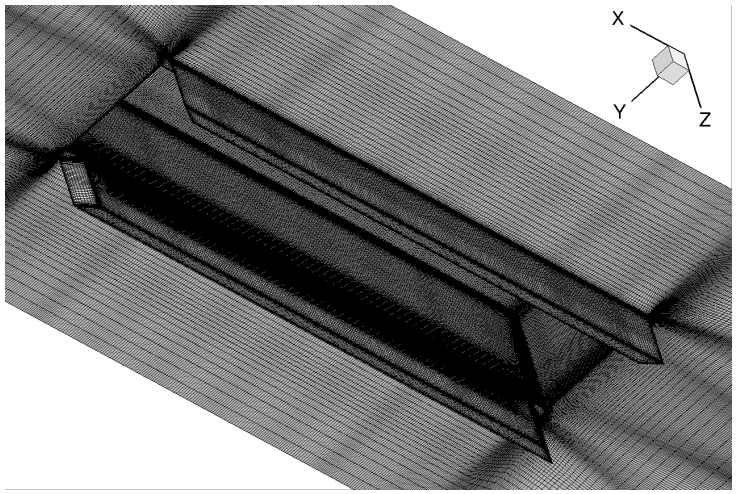

(c) Surface mesh - Fine grid

Figure 3: Schematic view of the M219 cavity with doors.

5 Validation of the CFD code

The time averaged C_p (Figure 4a) at the ceiling, and at the mid-span of the cavity, shows the grid convergence, with negligible changes between the different grid densities. The OASPL, on figure 4b is shown for the M219 cavity with doors. Since the CFD simulations are run for a typical length of 25 travel times, and the experimental data span 1900 travel times, the

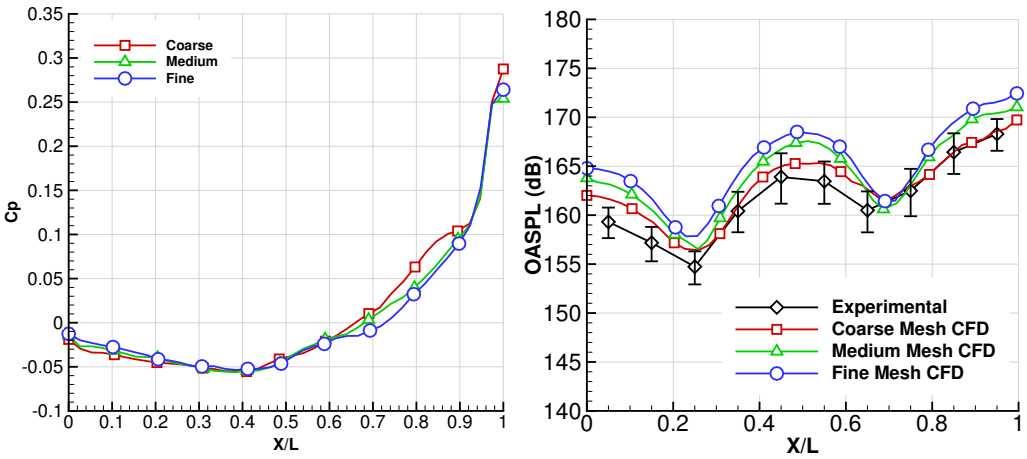

(a) Mean C_p (b) OASPL

Figure 4: OASPL, and mean C_p along the M219 cavity ceiling mid-span.

comparison is carried out as follows. The experiment is divided in windows of 25 travel time, and the result leads to the vertical bars shown with the OASPL. The second Rossiter mode is dominant, with a W shape, captured by the CFD and the experiments. The passage from medium to fine grid leads to a small noise increase of 1dB.

Figure 5 shows the SPL comparison between CFD and experiments at three points at 5%L, 45%L, and 95%L of the cavity mid-span, and on the ceiling. The SPL envelop is computed as the vertical bars of the OASPL, and the vertical lines are the Rossiter modes. The SPL shows better agreement with the test data when the fine grid is used, capturing both the tones and the broadband noise.

Figure 6, CFD is compared with the experiments for the cavity without

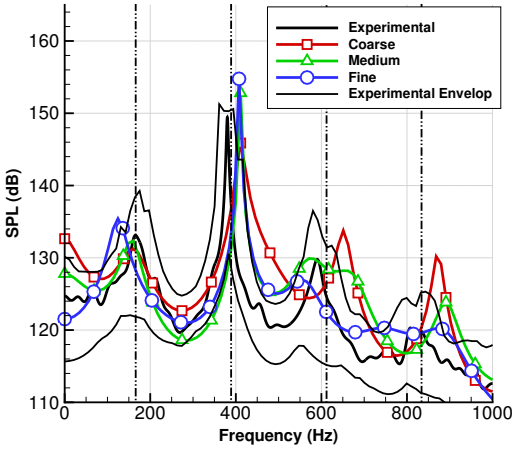

(a) X/L=0.05

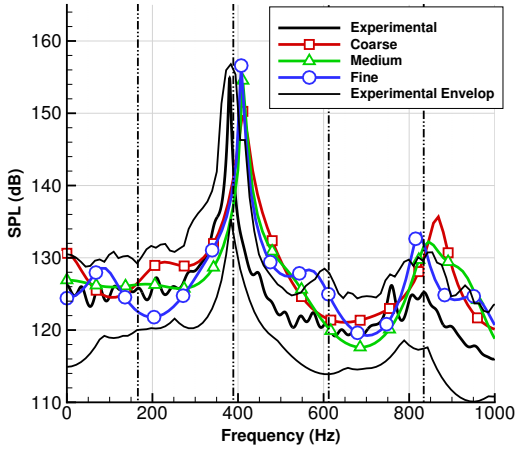

(b) X/L=0.45

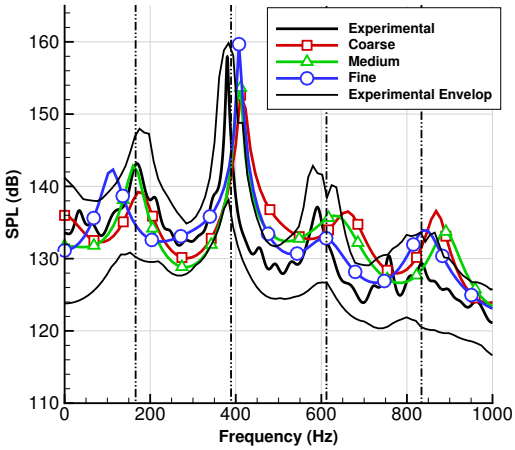

(c) X/L=0.95

Figure 5: SPL at the M219 cavity with door at the ceiling mid-span for CFD and experimental signals.

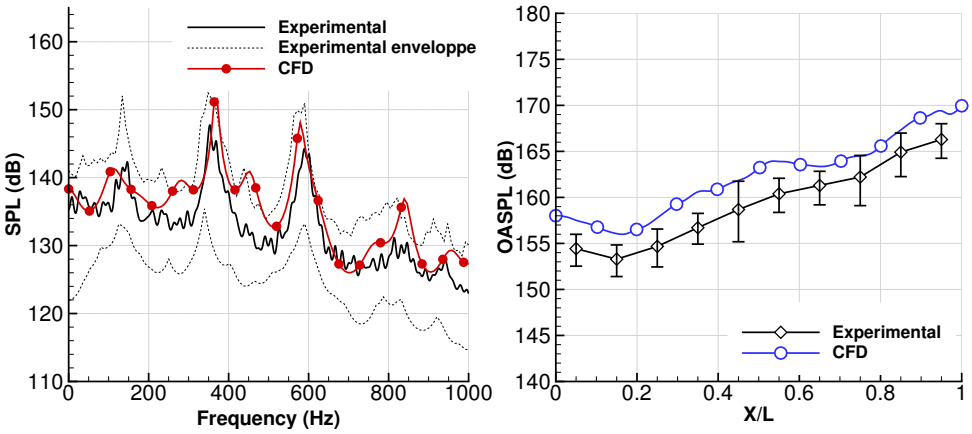

(a) SPL (b) OASPL

Figure 6: Noise along the no doors M219 cavity ceiling mid-span.

doors. Overall, the CFD captured well the differences between the door and no door configurations, including the strong increase of the second cavity mode with the doors on. The frequencies of the tones also agrees with the test data and Rossiter equation. This suggests that SAS is a suitable method to capture the essential physics of the flow (tones and broadband), and the effect of the doors. Both cases with and without doors show an overestimation of the OASPL, all along the cavity length. A large number of simulations performed with various models [30, 31, 32] shown a similar overestimation that may also be due to experimental errors, as well as limitations of the SAS and DES approaches.

In the following, the fine mesh density is used, and a length to depth ratio of 7 is adopted to be closer to actual weapon bay geometries.

6 Results and Discussions

6.1 Computations Static Doors

Figure 7 shows the time-averaged Mach Number on a plane at 85% of the cavity length for the LD7 cavity with and without doors. Over the clean cavity, the shear layer deeps in, reaching large depths of penetration (Figure 7a), and creating large structures above the side walls. Adding doors at 110 degrees, the shear layer is lifted (Figure 7b), reducing the Mach number inside the cavity. Decreasing the door angle, a further reduction of the Mach number is seen, and the doors at 20 degrees show negligible flow inside the cavity (Figure 7e).

The blockage of the flow by the doors is also visible in the OASPL in figure 8a. The doors at 110 degrees have a negligible effect on the OASPL when compared to a cavity without doors. Reducing the door angle, a pacifying effect appears, leading to the reduction of the sound pressure level by up to 20dB at 20 degrees. The addition of the doors at 90 degrees on the M219 cavity, has dramatically different consequences, with a stronger second cavity mode, seen on the W shape of the OASPL (Figure 8b), and an overall noise increase. This difference is due to the geometry of the door leading edge, that leads to different flowfield over the cavity for the two cases. This is shown in figure 9 with bottom view of the RMS of longitudinal velocity at the middle section of the doors. The M219 door pushes the flow above the cavity (Figure 9a), while the LD7 door is thinner, and pushes less flow above the cavity (Figure 9b). This leads to more pronounced flow fluctuations for

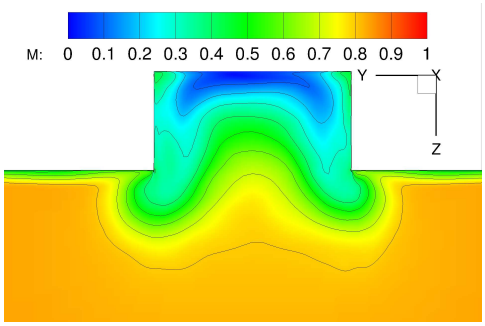

(a) No doors - Clean

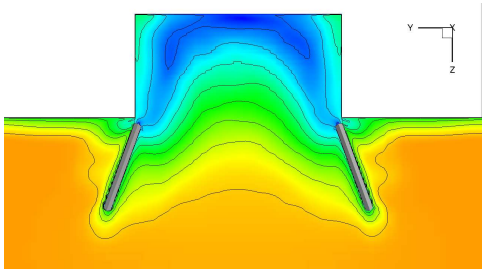

(b) 110 degrees - Clean

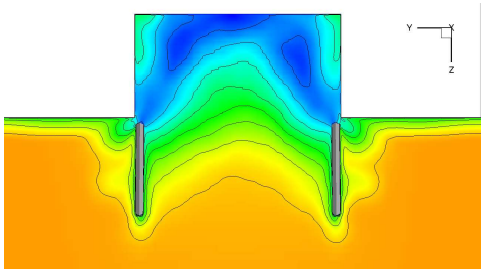

(c) 90 degrees - Clean

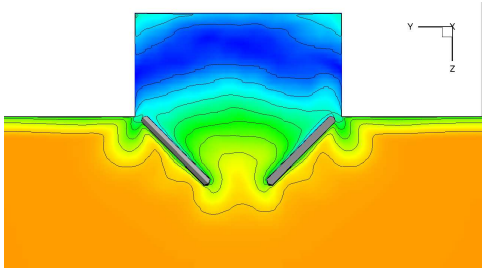

(d) 45 degrees - Clean

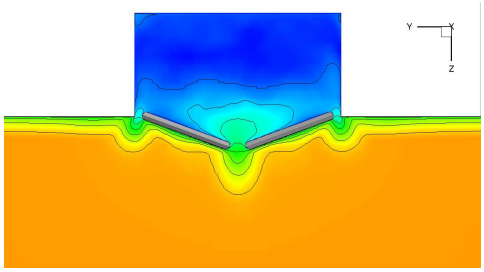

(e) 20 degrees - Clean

Figure 7: Mean Mach Number at X/L=0.85 for the LD7 cavity.

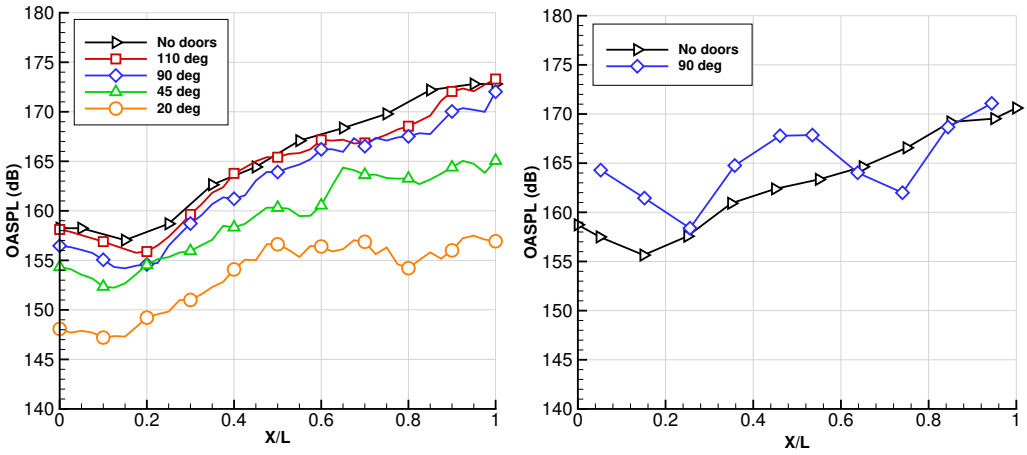

(a) LD7 cavity (b) M219 cavity

Figure 8: OASPL along the cavity ceiling mid-span.

the M219 cavity.

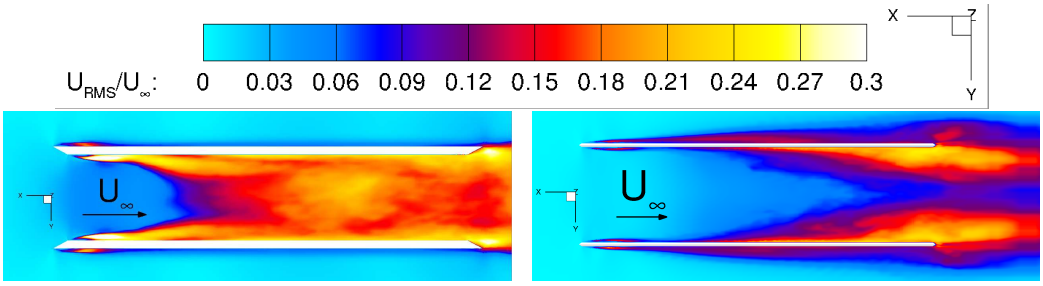

(a) M219 (b) LD7 with doors at 90 degrees

Figure 9: Time averaged U_{RMS} at the middle section of the doors.

Figure 10 shows the shear layer momentum of the time averaged flow for the LD7 and M219 cavities, with and without doors at 90 degrees. The two cavities have similar shear layer pattern without doors, with a thickness of the same order of magnitude compared to the cavity depth on the second half

of the cavity. Adding the doors, the M219 shear layer is lifted, and shows a dramatic reduction of its thickness compared to the LD7 cavity. The smaller width of the M219 cavity enhances the effect of the doors, leading to larger changes at the mid-span. This shows that the doors, strongly affect the cavity flow.

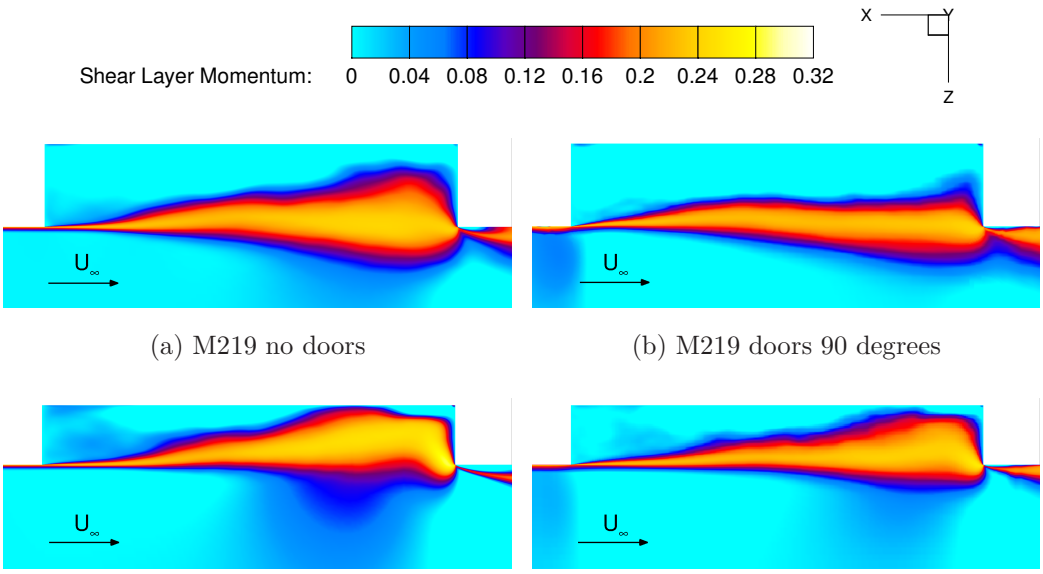

(a) M219 no doors

(b) M219 doors 90 degrees

(c) LD7 no doors

(d) LD7 doors 90 degrees

Figure 10: Shear layer momentum of the time averaged flow on the cavity mid-span.

6.2 Computations for Dynamic Door Opening

In the following discussion, the terms open and closed cavity have the meaning discussed in [33]. In a closed cavity (Figure 11a), the flow-stream separates from the leading edge of the cavity, but does not have enough energy

to cross it. The flow attaches on the cavity ceiling, and separates further downstream to attach at the trailing edge. This topology creates two strong vortices at the front and at the aft of the cavity. In open cavities (Figure 11b), the free-stream flow separates at the leading edge, and bridges the cavity, before impacting the aft wall. This creates a large re-circulation inside the cavity.

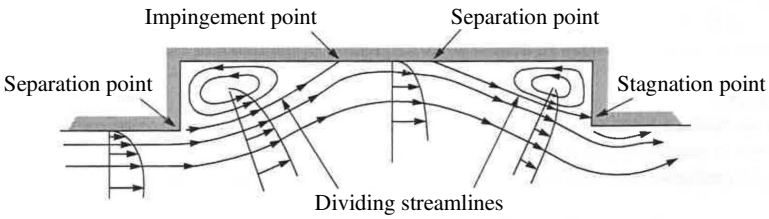

(a) Closed flow

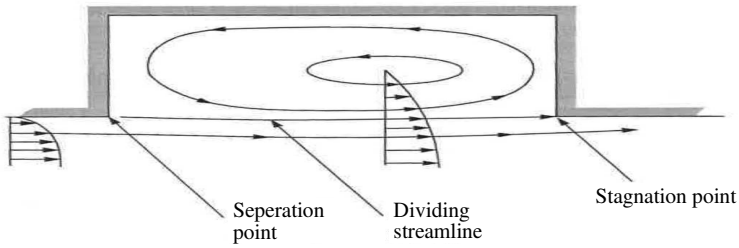

(b) Open flow

Figure 11: Schematic of open and closed cavity flow configurations at subsonic speeds[33].

The flows for dynamic, and static doors are compared in figure 12 using the Mach Number field, and the LICs (Linear Integral Convolution) [34]. The LIC algorithm applies a filter, based on an input vector field, to a noise

texture, producing an output image with the apparent motion in the direction of the vector field. The dynamic cases are averaged over windows of 10 degrees centred in the investigated angle. The static cases are averaged over the total time signal available. Figure 13 shows the forces on the front, and aft walls. The signals of the dynamic cases are averaged in windows of 1.6 travel times. The differences between min and max of the signal during the same window are also computed. Again, for the static cases, the full time signal is used.

For the dynamic opening cases, three phases are identified. First, the cavity flow adopts the closed cavity topology, then it transitions to an open cavity topology, and finally the flow becomes fully established, as the two doors stopped moving.

With the doors closed, the Mach Number inside the cavity is small, and the pressure is ambient (Figure 12a), showing that the gap between the doors and the bay discussed in section 4, did not influence the flow. As soon as the doors open, the flow enters in the cavity from a narrow gap between the doors and the cavity lips, creating a jet impacting the ceiling, and establishing a closed cavity flow (Figure 12b). The jet induces a vortex at the front of the cavity, decreasing the pressure, and increasing suction on the front wall (Figure 13a). This force is identical for all dynamic cases, driven by the jet flow. During this phase, the aft wall is subject to smaller loads (Figure 13c).

The cavity flow then transitions to an open cavity [33]. The jet travels along the cavity ceiling, reaches the cavity aft, and detaches to hit the aft wall, creating a peak of loads (Figures 12d and 13c). This weakens the vortex

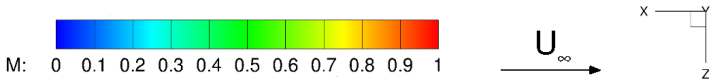

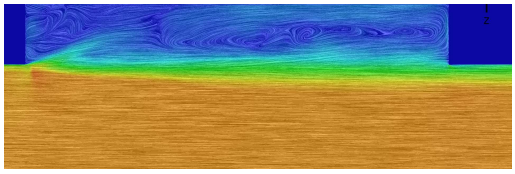

(a) Medium Speed - 5 degrees

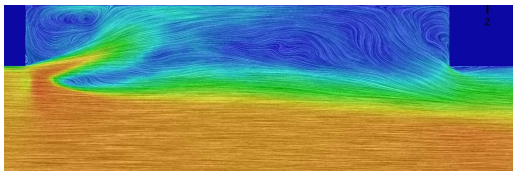

(b) Medium Speed - 20 degrees

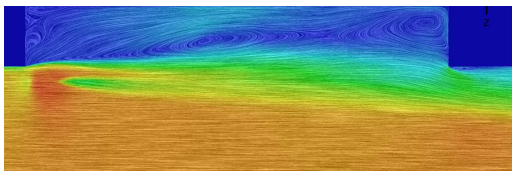

(c) Static - 20 degrees

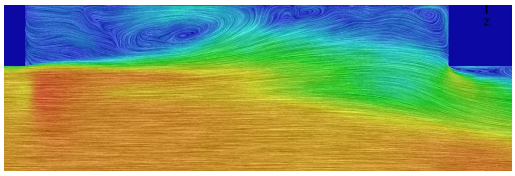

(d) Medium Speed - 35 degrees

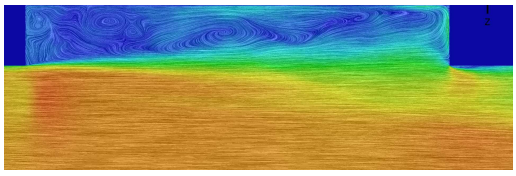

(e) Medium Speed - 45 degrees

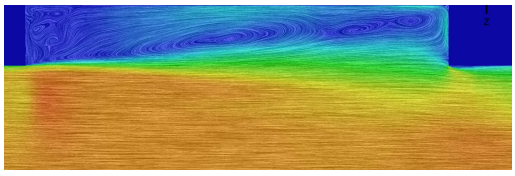

(f) Static - 45 degrees

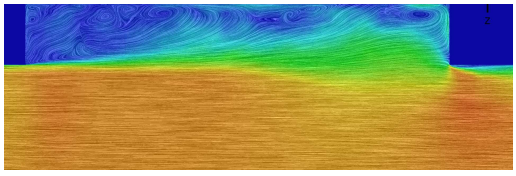

(g) Medium Speed - 90 degrees

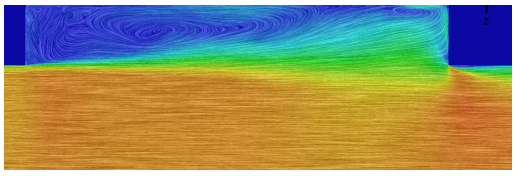

(h) Static - 90 degrees

Figure 12: Mach Number and LICs between 5 and 90 degrees for dynamic and static cases.

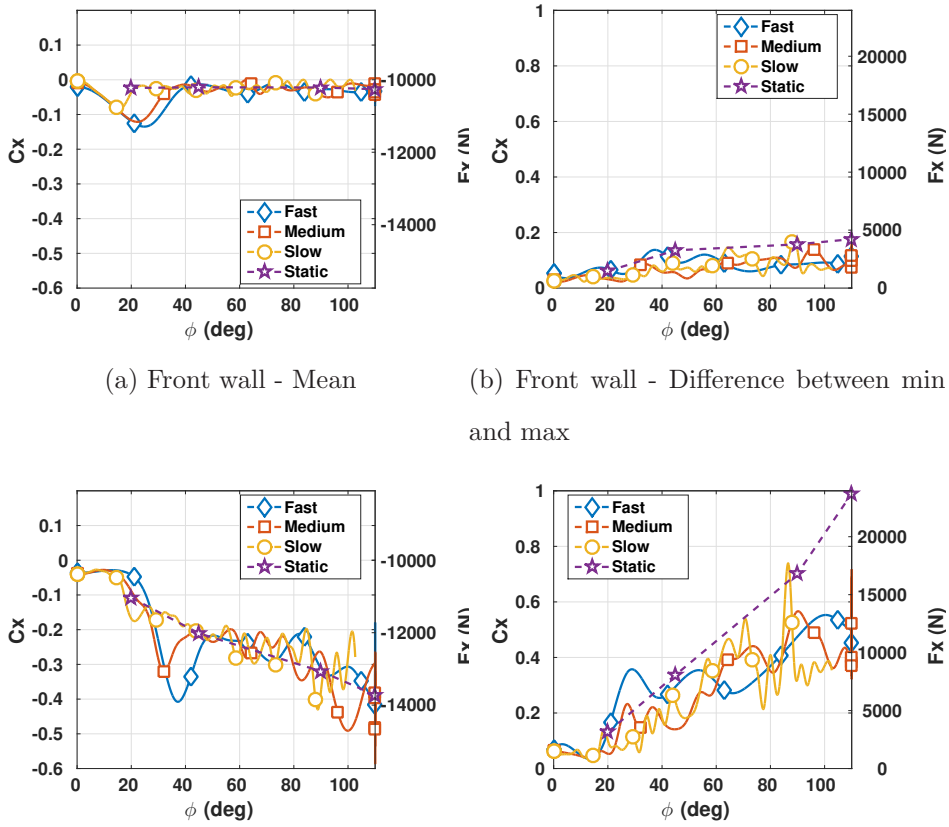

(a) Front wall - Mean

(b) Front wall - Difference between min and max

(c) Aft wall - Mean

(d) Aft wall - Difference between min and max

Figure 13: Force on the front and aft walls for static and dynamic doors.

near the front wall at different door angles according to the door velocity. The stronger front wall vortex is seen at 16, 23, and 25 degrees for the slow, medium, and fast doors (Figure 13a). The transition ends when the dynamic cases reach the same level of loads as the static cases. The faster the door, the larger the loads, and the fluctuations during the transition phase (Figure 13d).

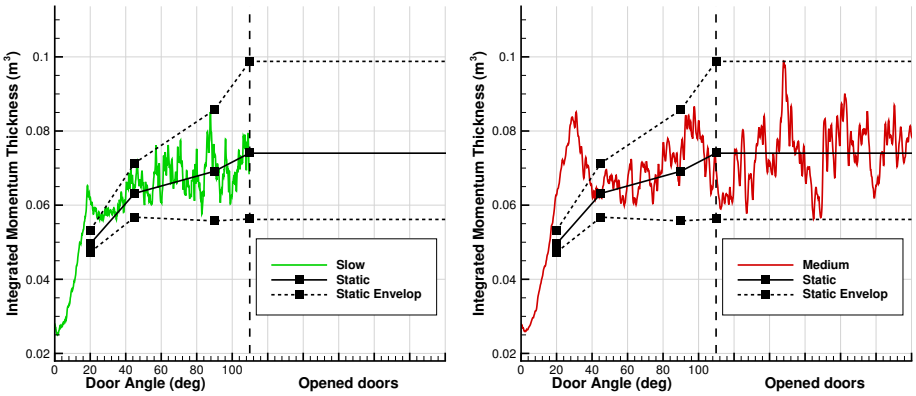

(a) Slow

(b) Medium

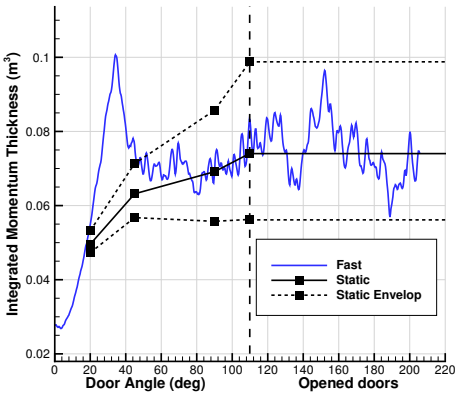

(c) Fast

Figure 14: Shear layer momentum thickness $\theta(x, y)$ integrated over the cavity opening.

Figure 14 shows the volume of the shear layer, computed as the integral of the shear layer momentum thickness $\theta(x, y)$ all over the cavity length, and span. The static cases are drawn in black with their time averaged, minimum, and maximum values. The narrower door opening limits the flow

development for this geometry, leading to smaller thickness and fluctuations of the shear layer. The dynamic cases show the footprint of the jet during the transitional phase, with a peak of the shear layer thickness. Then, all the dynamic cases are within the envelop defined by the static cases.

Figure 15 shows the pitching moment (Figures 15a to 15c) and the normal panel force (Figures 15d to 15f) on the left door, and the wall normal force

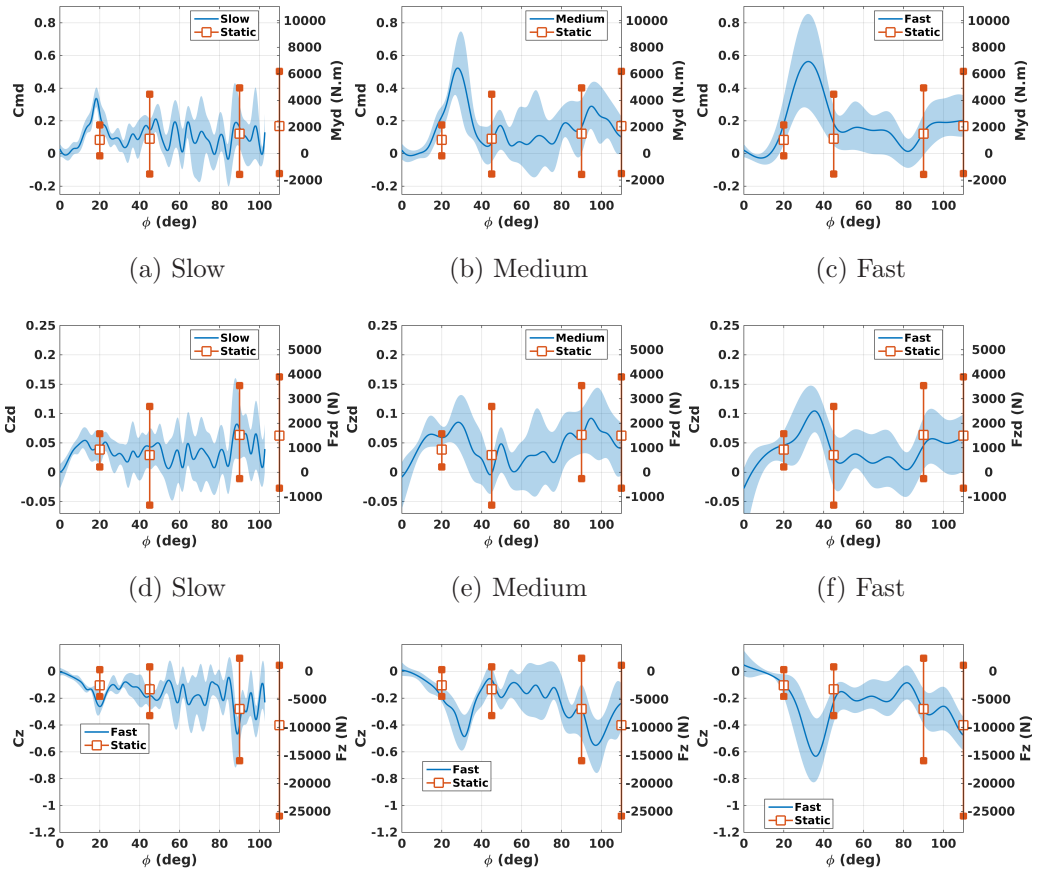

(a) Slow (b) Medium (c) Fast

(d) Slow (e) Medium (f) Fast

(g) Slow (h) Medium (i) Fast

Figure 15: Loads on doors and cavity ceiling for dynamic and static cases.

on the ceiling (Figures 15g to 15i). The coloured envelop is the minimum and maximum of the signal within windows of 1.6 travel time. The flow transition from open to closed topology, may affect stores inside the weapon bay. This is because larger transient loads are observed when compared to the fully opened bay, especially for the faster case. The maximum pitching moment on the doors during the fast opening (Figure 15c) is twice as large as for the fully open case.

6.3 Noise Field for Dynamic and Static Door Cases

Figure 16 shows the OASPL at the mid-plane of the cavity for the medium door speed, and for the cases with static doors. For small door openings, the jet produces high levels of noise at the front of the cavity (Figure 16b), and makes the dynamic case noisier than the static case (Figure 16c). The flow transition is also very noisy (Figure 16d), and resembles the fully open door cavity (Figure 16i). For larger door angles, the door dynamics has minimal influence on the noise field, with two main sources of noise at the mid-length of the shear layer, and at the aft wall.

The OASPL in the mid-span of the cavity, and averaged along the ceiling (Z/D=-1), as well as at the shear layer (Z/D=0), and at Z/D=1 are shown in figure 17, as functions of the door angle. At the ceiling, and outside the cavity, the dynamic cases show a peak of noise due to the flow transition. After the transition phase, the noise fields between static and dynamic openings are similar. The fast doors produce noise levels as loud as the fully open cavity

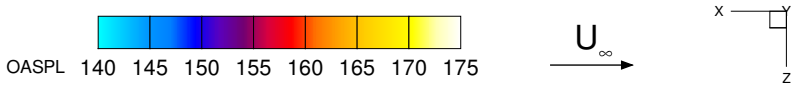

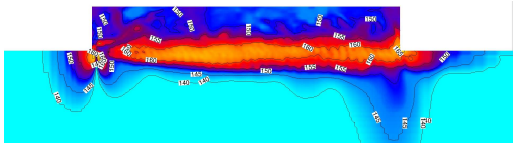

(a) Medium Speed - 5 degrees

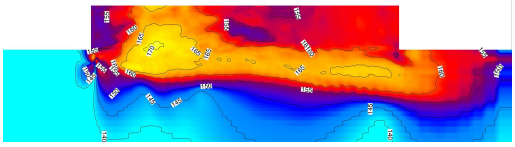

(b) Medium Speed - 20 degrees

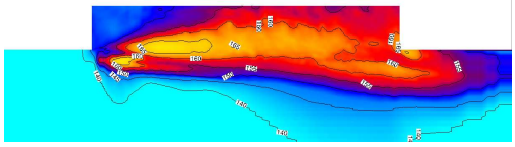

(c) Static - 20 degrees

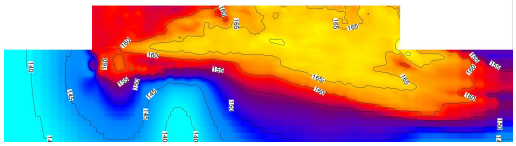

(d) Medium Speed - 35 degrees

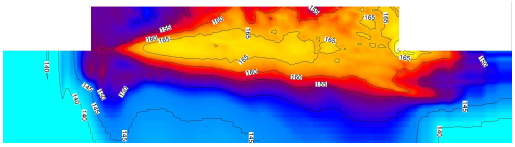

(e) Medium Speed - 45 degrees

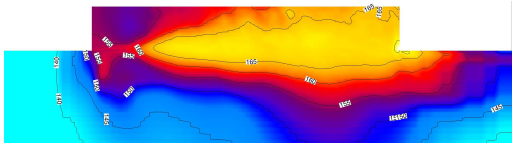

(f) Static - 45 degrees

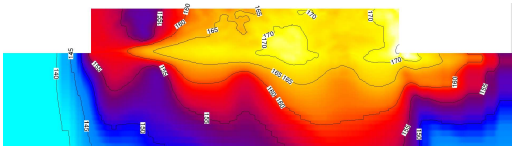

(g) Medium Speed - 90 degrees

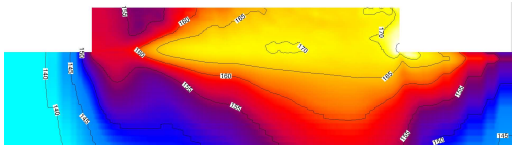

(h) Static - 90 degrees

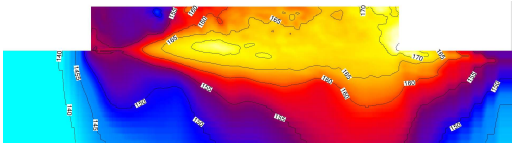

(i) Medium Speed - 110 degrees

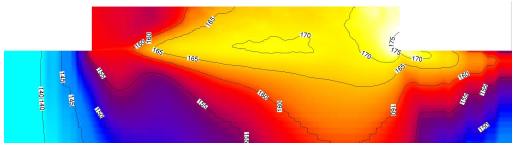

(j) Static - 110 degrees

Figure 16: OASPL field during the doors opening between 5 and 110 degrees.

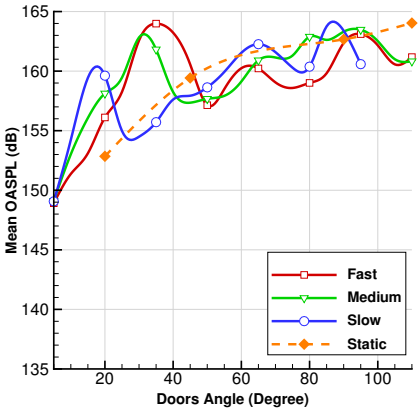

(a) Ceiling (Z/D=-1)

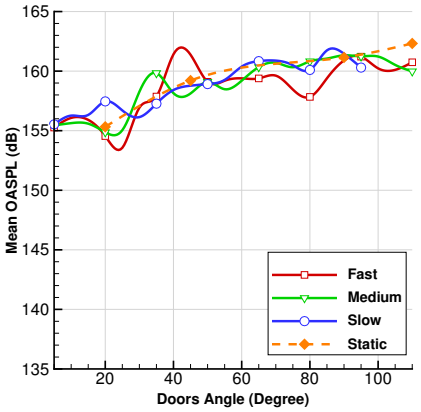

(b) Cavity opening (Z/D=0)

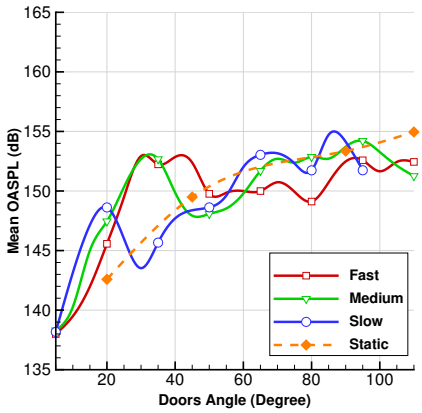

(c) One cavity depth (Z/D=1)

Figure 17: Averaged OASPL lines at the mid-span for fast, medium, slow, and static doors cases.

during the transition. At the shear layer (Figure 17b), the noise is produced by a whittling effect for the smaller angles (Figure 16a). Then, the noise levels increase as the shear layer establishes towards the end of the transition phase (Figure 16e).

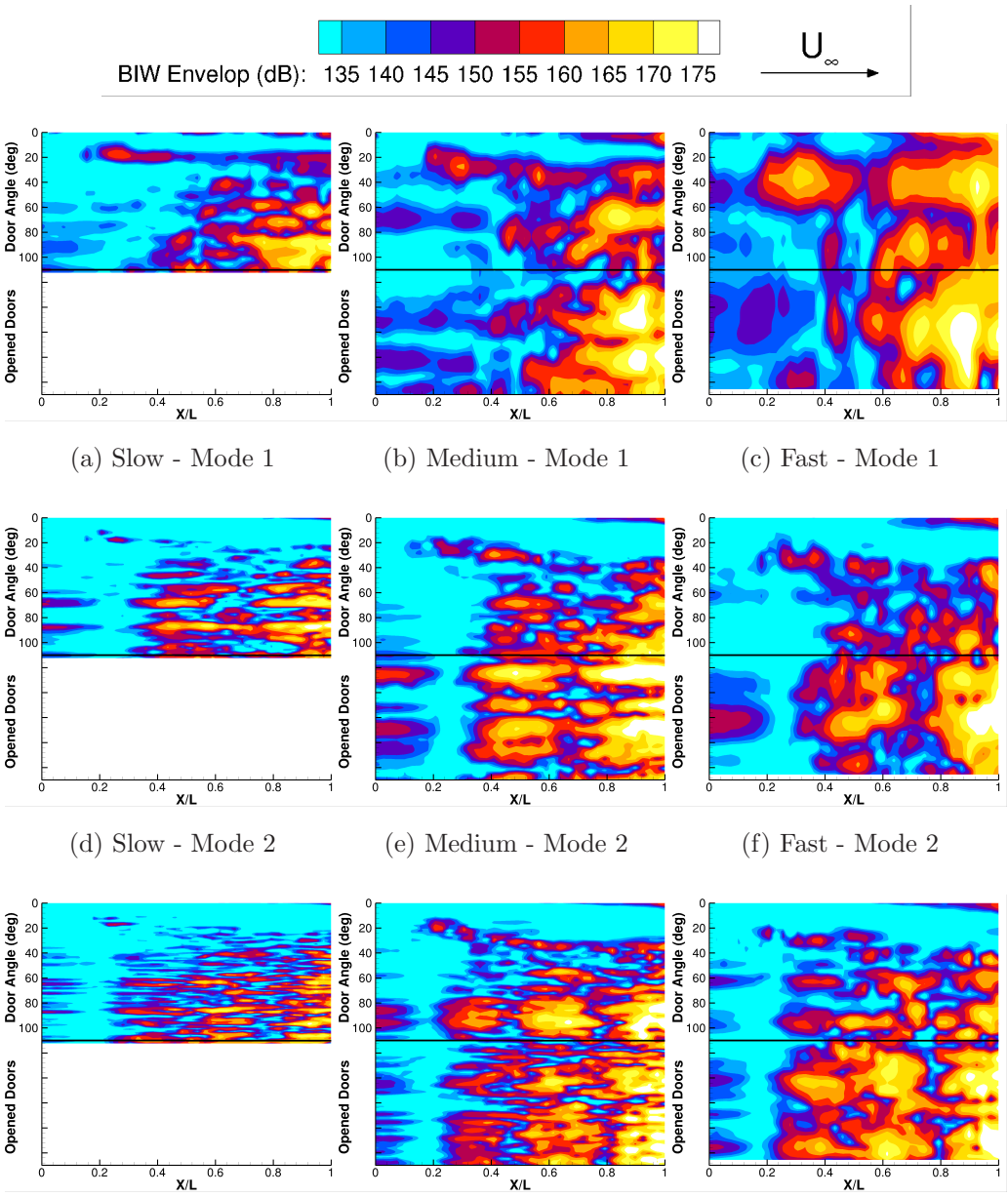

(a) Slow - Mode 1 (b) Medium - Mode 1 (c) Fast - Mode 1

(d) Slow - Mode 2 (e) Medium - Mode 2 (f) Fast - Mode 2

(g) Slow - Mode 3 (h) Medium - Mode 3 (i) Fast - Mode 3

Figure 18: Pressure BIW envelope along the ceiling mid-span for dynamic opening and mode 1 to 3.

The cavity flow is very unsteady during the door opening, and spatio-temporal characterisation is needed to be fully understood. The pressure Banded Integrated Wavelet (BIW) envelop is shown for three door velocities (Figure 18). The vertical axis is the time scaled by the door angle, and the horizontal axis represents the coordinate along the ceiling mid-span of the cavity. Three frequency bands of 4Hz centred on the cavity modes 1 to 3 are shown. During the cavity flow transition, the jet path is visible around a door angle of 20 degrees, interacting with the ceiling from 20% of the cavity length, and travelling towards the aft wall. After a door angle of 80 degrees, all cases look similar. After the flow transitioned to closed cavity, the noise patterns, show for all modes, a succession of minima of noise called nodes, and of maxima of noise called antinodes. There are, respectively, 2, 3, and 4 antinodes, for modes 1, 2 and 3. In addition, there is a large gradient of noise across the cavity length, and a modulation in time of the modes amplitudes, that are characteristic of shallow cavity flows [3, 35, 2].

Figure 19 compares the SPL at X/L=0.95 on the ceiling mid-span between static doors at 110 degrees, and dynamic door opening. The dynamic door signal is processed between angles of 45 and 110 degrees, after the cavity flow transition. The cavity with fully open doors is characterised by strong cavity modes (modes 1, 2 and 3). During the slow and medium speed opening, those modes settle rapidly after the flow transition, and dominate the SPL. However, the broadband noise is weaker than for the fully developed case. On the other hand, the fast opening does not allow enough time for the flow to develop, and only the third cavity mode is visible. Table 4 shows the

frequency of the three first cavity modes of those cases. The door dynamics has a small effect on the modal frequencies, which lock rapidly to values close to the Rossiter frequencies.

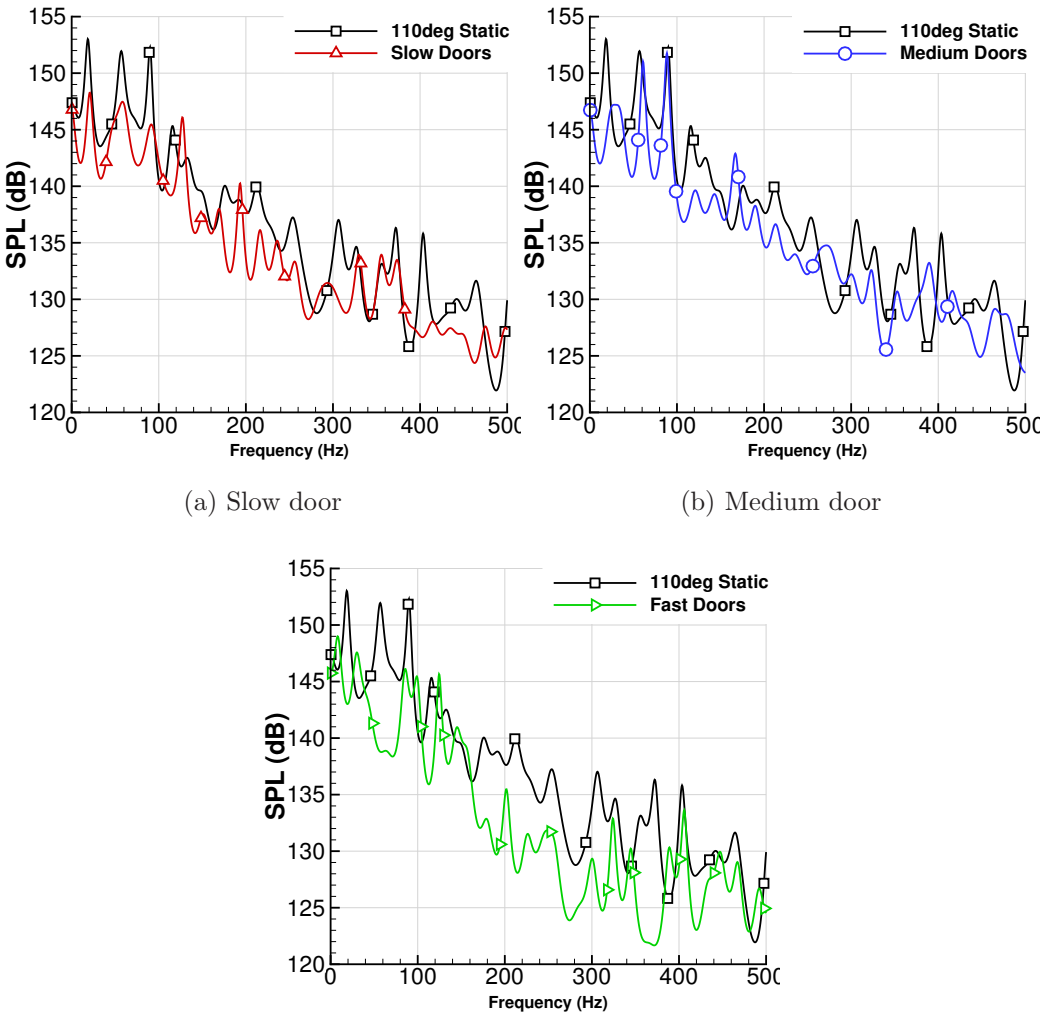

(a) Slow door

(b) Medium door

(c) Fast door

Figure 19: SPL at X/L=0.95 of the ceiling mid-span for different door speed.

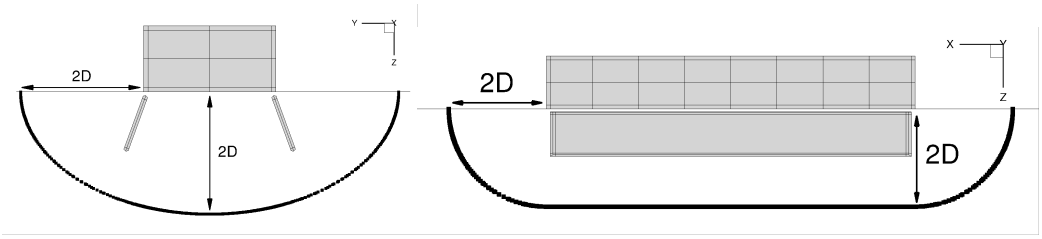

(a) Isosurface slice on YZ plane

(b) Isosurface slice on XZ plane

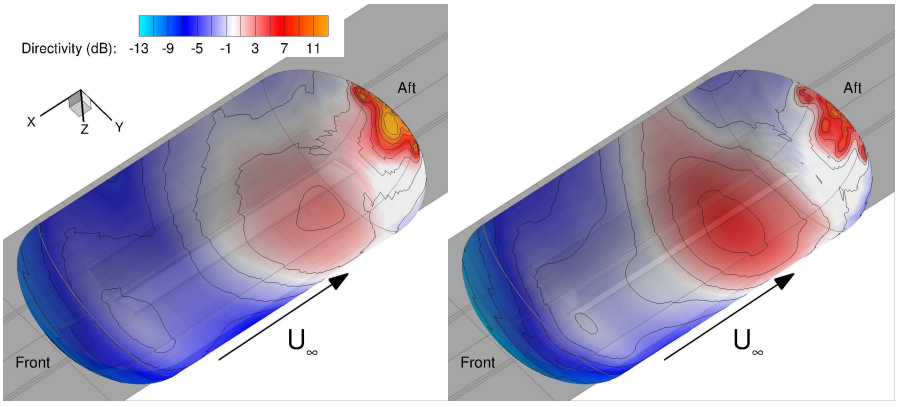

(c) 20 degree

(d) 45 degree

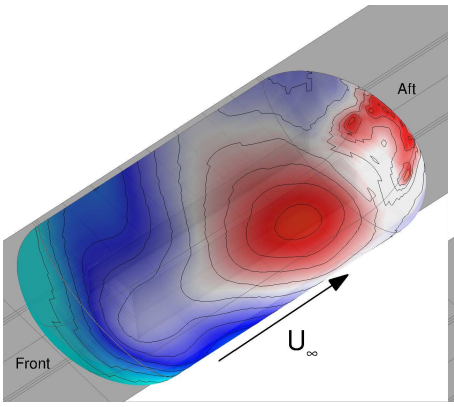

(e) 90 degree

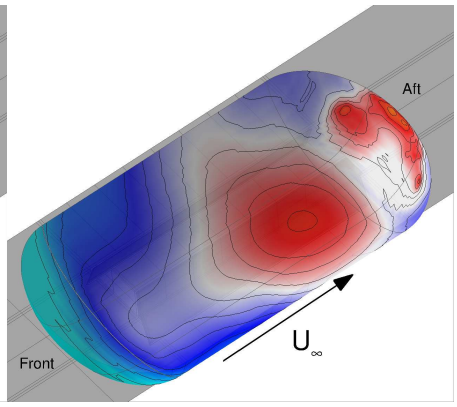

(f) 110 degree

Figure 20: 3D Noise directivity for different fixed door angle. Iso-surface at 2 cavity depths from the shear layer.

Case	Mode 1	Mode 2	Mode 3
Rossiter	23.7	55.2	86.8
Doors 110deg	19.1	57.6	89.7
Slow Doors	20.0	54.3	90.6
Medium Doors	19.5	60.2	88.0
Fast Doors	-	-	86.8

Table 4: Cavity mode frequency for dynamic and static doors in Hz.

Figure 20 describes the noise directivity at the cavity near field for different fixed door angles. Equation 14 is used on every CFD points of an iso-surface two cavity depths away from the cavity opening (Figures 20a and 20b). The mesh at the near field is fine enough to capture frequencies up to 466Hz with 10 points per wave length. The noise is directed at the aft and above the cavity as indicated by the peak values of 10dB. This may be explained by the loud noise at the cavity aft, generated as the shear layer impacts the aft wall. Additionally, the noise propagation is influenced by the advection by the transonic flow. This is visualised using a simple noise propagation model (Figure 21), where the speed of the pressure waves is the sum of the sound speed, and of the time averaged CFD flowfield velocity. Sources of noise are placed at the shear layer and at the aft wall, and radiate uniformly around them. For most of the sources placed in the flow, the waves are influenced by the flow direction, either the free-stream, or the recircula-

tion inside the cavity. As a result, most of the waves propagate downstream, and bellow the cavity in the Z direction.

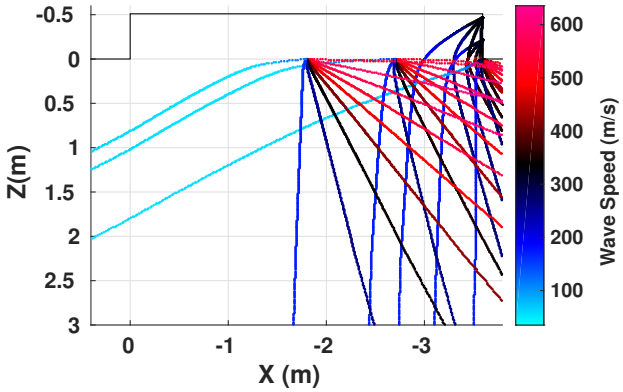

Figure 21: Noise propagation from the main sources of noise taking into account the flowfield with doors at 110 degrees.

Figure 22, shows iso-lines of acoustic directivity at the mid-span of the cavity, and at different door angles for the static cases, as well as for the slow and fast dynamic door cases. The dynamic cases are averaged in a window of 10 degrees around the indicated angle. The shapes of the static, and slow cases are similar past the 45 degrees door angle, as the cavity flow has time to establish. However, for the fast case, the shapes of the curves evolve, and fluctuate as the door opens.

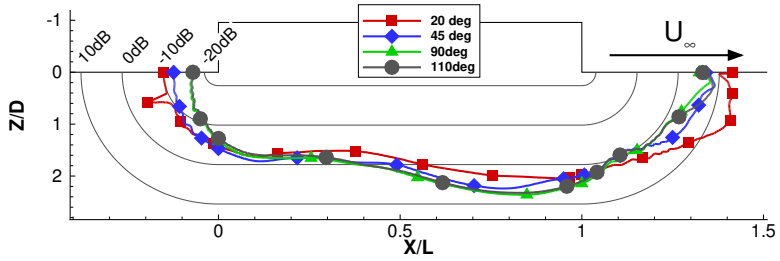

(a) Static

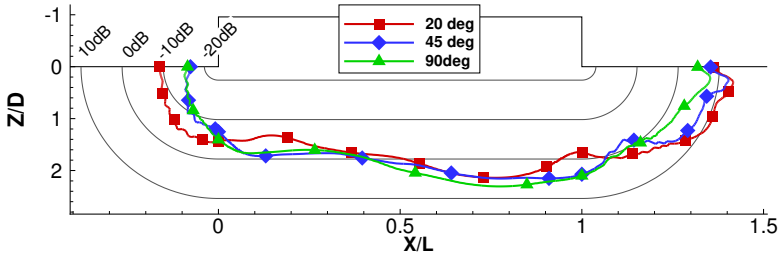

(b) Slow

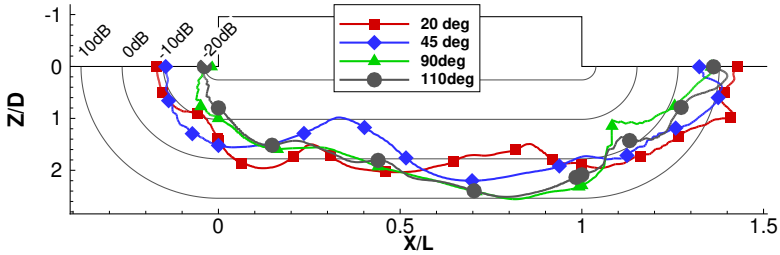

(c) Fast

Figure 22: Noise directivity for different door angle and door velocity.

7 Conclusions

This paper presented simulations of a transonic weapon bay flow with doors either fixed, or opened in a dynamic way. The door opening evolved in three stages. First, a closed cavity flow was established, with the creation of a jet, impacting the bay ceiling, and producing large fluctuations inside it. After, the flow became transitional, and the loads were amplified. The noise, as well as the flow fluctuations, were also larger than for the fully established flow. The faster doors, created the more unsteady flow during the opening. The flow during door opening may not influence the trajectory of a store released from the bay, as the flow has the time to reach a fully established state, before the releases initiated. However, the door opening has to be taken into account to design weapon bay structures, because of the larger peaks of loads seen during transition.

The doors used on the LD7 cavity had a pacifying effect on the cavity flow, while the M219 cavity doors, with a different design, amplified the cavity acoustics. This suggests that the door geometry can dramatically modify the cavity flow.

Future developments will focus on realistic bay geometries with doors operation, and store release.

Acknowledgments

The financial support of MBDA UK Ltd. is gratefully acknowledged. The use of the EPSRC funded ARCHIE-WeSt High Performance Computer (EPSRC

grant no. EP/K000586/1) is also gratefully acknowledged

References

[1] Schmit, R., Grove, J., Semmelmayer, F., and Haverkamp, M., "Nonlinear feedback mechanisms inside a rectangular cavity," *AIAA Journal*, Vol. 52, No. 10, 2014, pp. 2127 – 2142, doi:10.2514/1.J052804.

[2] Loupy, G. and Barakos, G., "Modelling of Transonic Shallow Cavity Flows and Store Release Simulations from Weapon Bays," *Proceedings of the 35th AIAA Applied Aerodynamics Conference*, Paper No. AIAA 2017-3252, American Institute of Aeronautics and Astronautics Inc, Denver, Colorado, United states, 2017, doi:10.2514/6.2017-3252.

[3] Rossiter, J. E., "Wind Tunnel Experiments on the Flow Over Rectangular Cavities at Subsonic and Transonic Speeds," Technical Report 64037, Royal Aircraft Establishment, Bedford, UK, October 1964.

[4] Lawson, S. and Barakos, G., "Review of Numerical Simulations For High-Speed, Turbulent Cavity Flows," *Progress in Aerospace Sciences*, Vol. 47, No. 3, 2011, pp. 186 – 216, doi:10.1016/j.paerosci.2010.11.002.

[5] Kannepalli, C., Chartrand, C., Birkbeck, R., Sinha, N., and Murray, N., "Computational modeling of geometrically complex weapons bays," *Proceedings of the 17th AIAA/CEAS Aeroacoustics Conference 2011*, Paper No. AIAA 2011-2774, American Institute of Aeronautics and Astro-

nautics Inc, Portland, Oregon, United States, 2011, doi:10.2514/6.2011-2774.

[6] Panickar, M., Murray, N., Jansen, B., Joachim, M., Birkbeckand, R., Kannepalli, C., and Sinha, N., "Reduction of noise generated by a half-open weapons bay," *Journal of Aircraft*, Vol. 50, No. 3, 2013, pp. 716 – 724, doi:10.2514/1.C031747.

[7] Casper, K., Wagner, J., Beresh, S., Hening, J., Spillers, R., and Pruett, B., "Complex Geometry Effects on Subsonic Cavity Flows," *Proceedings of the 53rd AIAA Aerospace Sciences Meeting*, Paper No. AIAA 2015-1291, American Institute of Aeronautics and Astronautics Inc, Kissimmee, Florida, United States, 2015, doi:10.2514/6.2015-1291.

[8] Barakos, G., Lawson, S., Steijl, R., and Nayyar, P., "Numerical Simulations of High–Speed Turbulent Cavity Flows," *Flow, Turbulence and Combustion*, Vol. 83, No. 4, December 2009, pp. 569–585, doi:10.1007/s10494-009-9207-1.

[9] Murray, N. and Jansen, B., "Effect of door configuration on cavity flow modulation process," *AIAA Journal*, Vol. 50, No. 12, 2012, pp. 2932 – 2937, doi:10.2514/6.2011-2773.

[10] Sheta, E., Harris, R., George, B., Ukeiley, L., and Luke, E., "Loads and Acoustics Prediction on Deployed Weapons Bay Doors," *Journal of Vibration and Acoustics, Transactions of the ASME*, Vol. 139, No. 3, 2017, doi:10.1115/1.4035701.

[11] Blair, A. and Stallings, R., "Cavity door effects on aerodynamic loads of stores separating from cavities," *Journal of Aircraft*, Vol. 26, No. 7, 1989, pp. 615 – 620, doi:10.2514/3.45811.

[12] Bacci, D., Saddington, A., and Bray, D., "Transient aerodynamics and aeroacoustics of complex-geometry weapon bays," *Proceedings of the 50th 3AF International Conference on Applied Aerodynamics*, Paper No. FP08-2015-bacci, La Société Savante de l'Aéronautique et de l'Espace, Toulouse, France, 2015.

[13] Menter, F. and Egorov, Y., "The Scale-Adaptive Simulation Method for Unsteady Turbulent Flow Predictions. Part 1: Theory and Model Description," *Flow, Turbulence and Combustion*, Vol. 85, No. 1, 2010, pp. 113–138, doi:10.1007/s10494-010-9264-5.

[14] Egorov, Y., Menter, F., Lechner, R., and Cokljat, D., "The Scale-Adaptive Simulation Method for Unsteady Turbulent Flow Predictions. Part 2: Application to Complex Flows," *Flow, Turbulence and Combustion*, Vol. 85, No. 1, 2010, pp. 139–165, doi:10.1007/s10494-010-9265-4.

[15] Babu, S., Zografakis, G., and Barakos, G., *Evaluation of scale-adaptive simulations for transonic cavity flows*, *Progress in Hybrid RANS-LES Modelling: Papers Contributed to the 5th Symposium on Hybrid RANS-LES Methods, 19-21 March 2014, College Station, A&M University, Texas, USA*, edited by S. Girimaji, W. Haase, S.-H. Peng, and

D. Schwamborn, Vol. 130, Springer International Publishing, 2015, pp. 433–444, doi:10.1007/978-3-319-15141-0_35.

[16] Lawson, S. J., Steijl, R., Woodgate, M., and Barakos, G. N., "High performance computing for challenging problems in computational fluid dynamics," *Progress in Aerospace Sciences*, Vol. 52, No. 1, 2012, pp. 19–29, doi: 10.1016/j.paerosci.2012.03.004.

[17] Hirt, C. W., Amsten, A. A., and Cook, J. L., "An Arbitrary Lagrangian-Eulerian Computing Method for All Flow Speeds," *Journal of Computational Physics*, Vol. 14, No. 3, 1974, pp. 227–253, doi: 10.1006/jcph.1997.5702.

[18] Osher, S. and Chakravarthy, S., "Upwind Schemes and Boundary Conditions with Applications to Euler Equations in General Geometries," *Journal of Computational Physics*, Vol. 50, No. 3, 1983, pp. 447–481, doi:10.1016/0021-9991(83)90106-7.

[19] Roe, P., "Approximate Riemann Solvers, Parameter Vectors and Difference Schemes," *Journal of Computational Physics*, Vol. 43, No. 2, 1981, pp. 357–372, doi:10.1016/0021-9991(81)90128-5.

[20] van Leer, B., "Towards the ultimate conservative difference scheme. V.A second-order sequel to Godunov's Method," *Journal of Computational Physics*, Vol. 32, No. 1, 1979, pp. 101–136, doi:10.1016/0021-9991(79)90145-1.

[21] van Albada, G., van Leer, B., and Roberts, W., *A Comparative Study of Computational Methods in Cosmic Gas Dynamics*, *Upwind and High-Resolution Schemes*, edited by M. Y. Hussaini, B. van Leer, and J. Van Rosendale, Springer Berlin Heidelberg, Berlin, Heidelberg. Germany, 1997, pp. 95–103, doi:10.1007/978-3-642-60543-7_6.

[22] Axelsson, O., *Iterative Solution Methods*, Cambridge University Press, Cambridge, MA, United States, 1994, pp. 504–557, doi:10.1017/CBO9780511624100.

[23] Jameson, A., Schmidt, W., and Turkel, E., "Numerical Solutions of Euler Equations by Finite Volume Methods Using Runge-Kutta Time-Stepping Schemes," *Proceedings of the Fourteenth Fluid and Plasma Dynamic Conference*, Paper No. 1981-1259, American Institute of Aeronautics and Astronautics Inc, Palo Alto, CA, United States, 1981, pp. 1–19, doi:10.2514/6.1981-1259.

[24] Jarkowski, M., Woodgate, M., Barakos, G., and Rokicki, J., "Towards Consistent Hybrid Overset Mesh Methods for Rotorcraft CFD," *International Journal for Numerical Methods in Fluids*, Vol. 74, No. 8, 2014, pp. 543–576, doi:10.1002/fld.3861.

[25] Babu, S., Loupy, G., Dehaeze, F., Barakos, G., and Taylor, N., "Aeroelastic simulations of stores in weapon bays using Detached-Eddy Simulation," *Journal of Fluids and Structures*, Vol. 66, October 2016, pp. 207–228, doi:10.1016/j.jfluidstructs.2016.07.014.

[26] Pierce, A., *Acoustics: An Introduction to its Physical Principles and Applications*, Woodbury, New York: Acoustical Society of America, 1989.

[27] Heller, H., Holmes, D., and Covert, E., "Flow-Induced Pressure Oscillations In Shallow Cavities," *Journal of Sound and Vibration*, Vol. 18, No. 4, 1971, pp. 545 – 553, doi:10.1016/0022-460X(71)90105-2.

[28] Bussow, R., "An algorithm for the continuous Morlet wavelet transform," *Mechanical Systems and Signal Processing*, Vol. 21, No. 8, 2007, pp. 2970–2979, doi:10.1016/j.ymssp.2007.06.001.

[29] Nightingale, D., Ross, J., and Foster, G., "Cavity Unsteady pressure measurements - Examples from Wind-Tunnel Tests," Tech. Rep. Version 3, Aerodynamics & Aeromechanics Systems Group, QinetiQ, Bedford, UK, November 2005.

[30] Allen, R., Mendona, F., and Kirkham, D., "RANS and DES turbulence model predictions of noise on the M219 cavity at M=0.85," *International Journal of Aeroacoustics*, Vol. 4, No. 1, 2015, pp. 135–151, doi:10.1260/1475472053730039.

[31] Peng, S.-H., *M219 Cavity Flow*, *DESider A European Effort on Hybrid RANS-LES Modelling*, edited by W. Haase, M. Braza, and A. Revell, Vol. 103, Springer International Publishing, 2009, pp. 270–285, doi:10.1007/978-3-540-92773-0.

[32] Temmerman, L., Tartinville, B., and Hirsch, C., *URANS Investigation of the Transonic M219 Cavity*, *Progress in Hybrid RANS-LES Mod-*

elling: Papers Contributed to the 4th Symposium on Hybrid RANS-LES Methods, Beijing, China, September 2011, edited by S. Fu, W. Haase, S.-H. Peng, and D. Schwamborn, Springer Berlin Heidelberg, Berlin, Heidelberg, 2012, pp. 471–481, doi:10.1007/978-3-642-31818-4_41.

[33] Chappell, P. and Gilbey, R. W., "Drag of a rectangular planform cavity in a flat plate with a trubulent boundary layer for Mach numbers up to 3. Part II: Open and transitional flows." Tech. Rep. ESDU 00007, London, UK, February 2002.

[34] Cabral, B. and Leedom, L., "Imaging Vector Fields using Line Integral Convolution," *Proceedings of the 20th annual conference on Computer graphics and interactive techniques, SIGGRAPH*, ACM, Anaheim, CA, United States, 1993, pp. 263–270.

[35] Kegerise, M., Spina, E., Garg, S., and Cattafesta, L., "Mode-Switching and Nonlinear Effects In Compressible Flow Over a Cavity," *Physics of Fluids*, Vol. 16, No. 3, 2004, pp. 678–687, doi:10.1063/1.1643736.